Journal of Alloys and Compounds 970 (2024) 172541

Contents lists available at ScienceDirect

Journal of Alloys and Compounds

journal homepage: www.elsevier.com/locate/jalcom

Anisotropic plasticity mechanisms in a newly synthesised high entropy alloy investigated using atomic simulations and nanoindentation experiments

Pengfei Fan [a], Nirmal Kumar Katiyar [a,b], Muhammad Arshad [c], Mingwen Bai [d], Hui Mao [e], Saurav Goel [a,f,*]

[a] London South Bank University, 103 Borough Road, London, SE1 0AA, UK
[b] Amity Institute of Applied Sciences, Amity University Noida, 201303, India
[c] Centre for Manufacturing and Materials, Coventry University, Coventry, CV1 5FB, UK
[d] School of Mechanical Engineering, University of Leeds, Leeds, LS2 9JT, UK
[e] Department of Chemical Engineering, Imperial College London, London, SW7 2AZ, UK
[f] University of Petroleum and Energy Studies, Dehradun, 248007, India

ARTICLE INFO

Keywords:
High entropy alloy
Deformation behaviour
Grain boundaries
Nanoindentation
MD simulations

ABSTRACT

This work used atomic simulations and nanoindentation experiments to investigate hardness, modulus alongside sub-surface crystal defects and dislocation mediated plasticity mechanisms leading to anisotropic pile up and local entropy variation in high entropy alloys. The experimental campaign began from Thermo-Calc phase prediction of $Ni_{25}Cu_{18.75}Fe_{25}Co_{25}Al_{6.25}$ HEA which followed experimental synthesis of the material using arc melting method and experimental nanoindentation using a Berkovich indenter under load-controlled conditions. Through MD simulations, the value of h_f/h_{max} in monocrystalline HEA was consistently found to be larger than 0.7 which suggested pile-up behaviour to dominate and sink-in behaviour to be unlikely. In the case of (110) and polycrystalline HEA substrates, the elastic work in the indentation hysteresis loop was seen to be larger than the (100) and the (111) orientations which explains that the (110) orientation substrate showed least elastic modulus and hardness while the (111) monocrystalline HEA showed the highest elastic modulus and hardness. From the simulations, a "lasso" type loop on the (110) orientation and cross-over of shear loops on the other orientations accompanied by dislocations of type 1/6 < 112 > (Shockley), 1/2 < 110 > (perfect), 1/3 < 001 > (Hirth), 1/6 < 110 > (Stair rod) and 1/3 < 111 > (Frank partials) were seen to manifest an early avalanche of competing plasticity events. The defects accompanying these dislocations in the sub-surface were identified to be FCC intrinsic stacking faults (ISF), adjacent intrinsic stacking faults (quad faults), coherent $\sum 3$ twin boundary and a coherent twin boundary next to an intrinsic stacking fault (triple fault). The EBSD analysis applied to the MD data showed that the (210) orientation and the< 110 > family of directions were seemed to be preferable to plastically deform the FCC phased $Ni_{25}Cu_{18.75}Fe_{25}Co_{25}Al_{6.25}$ HEA.

1. Introduction

High-entropy alloys (HEAs) have attracted remarkable attention due to their excellent mechanical properties such as high strength and ductility [1–3], excellent fracture toughness [4,5] and stability at both cryo-temperature and at high temperatures [6], corrosion resistance [7], radiation resistance and wear resistance [8–11]. These properties makes HEA an ideal engineering material for a wide range of applications in sectors ranging from nuclear [12], photothermal conversion [13], integrated circuits [14], aerospace high-pressure gas turbine engine [15] and many more.

To further enhance the gas and steam turbine efficiency in comparison with traditional Ni-based superalloys, recently, a new HEA $Ni_{25}Cu_{18.75}Fe_{25}Co_{25}Al_{6.25}$ has been reported through the machine learning method which was experimental synthesised using vacuum arc melting under inert gas environment [16]. Similar to other engineering materials, HEA also possess strong anisotropy, however, these aspects of anisotropic deformation behaviour of HEA have just begun to be

* Corresponding author at: London South Bank University, 103 Borough Road, London SE1 0AA, UK.
E-mail address: GoeLs@Lsbu.ac.uk (S. Goel).

https://doi.org/10.1016/j.jallcom.2023.172541
Received 7 August 2023; Received in revised form 12 September 2023; Accepted 15 October 2023
Available online 16 October 2023

investigated. This is important for instance, if HEA is being promoted for its use as a potential bond coating material for gas turbine engines, then deploying HEA with preferable orientation can improve coating lifetime. Also, it is unknown at this stage whether FCC phased HEAs and BCC phased HEAs follow same extent of anisotropy as monoatomic elemental metals such as copper (FCC) and Tantalum (BCC) or the presence of different type of atoms makes HEA behave differently during its plastic deformation?

Computation calculations offer new possibilities to obtain faster predictions about the material behaviour. On this front, the use of machine learning and data driven models, offer new avenues and much work in this area is being undertaken at present [16]. On the contrary, atomistic computational tools such as molecular dynamics (MD) simulation use physics-based rationale to provide theoretically accurate predictions. Researchers can now use MD to probe crystal defects, dislocation mediated plasticity and preferential directions of deformation with a greater level of certainty [17,18]. On course to such an investigation, a recent study investigated the influence of alloy composition and grain size on the mechanical behaviour of AlCoCrFeNi HEA [19]. However, this study did not focus on investigating anisotropy in HEA. Similarly, another MD simulation was employed to investigate FeNiCrCoCu HEA and it reported about the complementary roles of dislocation activity and twinning in controlling plasticity during nanoindentation response [20].

These studies provides a good basis to build on the initial work and in that process, it is the first investigation which provides a comparison of the MD simulation with the nanoindentation experiments on $Ni_{25}Cu_{18.75}Fe_{25}Co_{25}Al_{6.25}$ high entropy alloy to better understand the anisotropic behaviour during nanoindentation.

2. Experimental and simulation setup

2.1. Experimental synthesis and nanoindentation of $Ni_{25}Cu_{18.75}Fe_{25}Co_{25}Al_{6.25}$ alloy

2.1.1. Theoretical phase prediction of HEA

The CALPHAD methodology was utilised to minimise the global Gibbs free energy of a multicomponent system as a function of temperature and composition, thereby enabling the prediction of phase equilibria for $Ni_{25}Cu_{18.75}Fe_{25}Co_{25}Al_{6.25}$. To visually represent the phase equilibria of this alloy in terms of phase percent as a function of temperature, a one-dimensional step diagram was employed using Thermo-Calc software (2023a) with TCHEA6 database [21], as shown in Fig. 1.

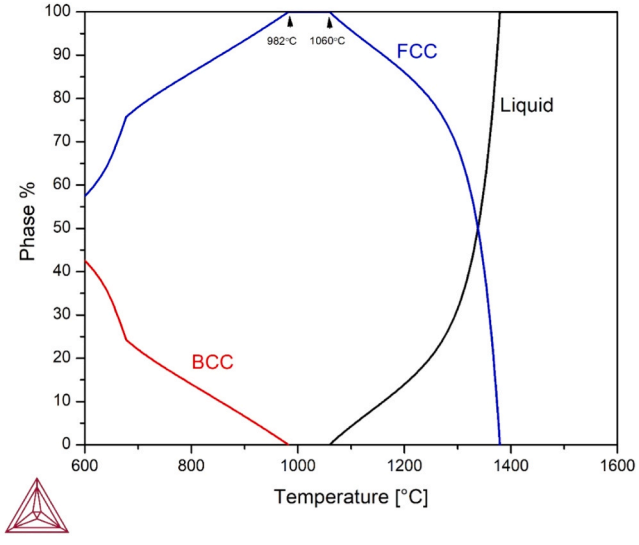

Fig. 1. Phase composition of $Ni_{25}Cu_{18.75}Fe_{25}Co_{25}Al_{6.25}$ alloy as a function of temperature calculated by Thermo-Calc software with TCHEA6 database.

Fig. 1 shows key characteristics of the phase equilibria, including the width of the single-phase face-centred cubic (FCC) region of the high-entropy alloy (HEA) spanning from the solvus to the solidus at 1380 °C down to a lower temperature. Additionally, the diagram illustrates the appearance of a body-centred cubic (BCC) phase at intermediate temperatures. The as-cast alloys contains inhomogeneities that arise from the partitioning of slow-diffusing/high-melting point elements from fast-diffusing/low-melting point elements [22]. These inhomogeneities introduce variations not only in the composition but also in the solidus (incipient melting) temperature. The equilibrium diagram illustrates the phases that emerge when the alloy is annealed at a sufficiently high temperature for a long duration to allow for complete atomic diffusion and the attainment of the most thermodynamically stable configuration with the lowest possible Gibbs free energy. The CALPHAD approach plays a critical role in predicting the compositional evolution during solidification by coupling databases of thermodynamic parameters with diffusional kinetics parameters.

2.1.2. Experimental synthesis of HEA

To begin the experimental synthesis, the metal buttons were procured. Various metal buttons of Ni, Cu, Fe, Co and Al elements (purities> 99.99%) were purchased from Thermofisher Scientific®. All elemental metals were melted together by vacuum arc melting under inert gas (high purity Ar) environment. The ingot formed in the process was melted and solidified multiple times to ensure chemical homogeneity, and then the HEA button was vacuum sealed in a quartz tube, homogenised at 1000 °C for 10 h, and then quenched into water for stabilising high-temperature phase. The detailed description of this high-entropy alloy is provided in Table 1.

The specimen obtained from the experiments was a polycrystalline HEA with its composition $Ni_{25}Cu_{18.75}Fe_{25}Co_{25}Al_{6.25}$. The XRD examination of $Ni_{25}Cu_{18.75}Fe_{25}Co_{25}Al_{6.25}$ revealed face-centered cubic (FCC) structure as shown in Fig. 2. The supercell lattice parameter (lattice constant) of this alloy was determined to be 0.3615 nm. The XRD of the simulated HEA alloy is also shown for comparison and both plots confirmed crystalline FCC structure with similar lattice parameter.

2.1.3. Nanoindentation experiments on HEA

Nanoindentation experiments were conducted under load controlled conditions on a NanoTest Vantage machine (V5) machine from Micro-materials, UK. A Berkovich indenter tip (radius ~140 nm) was used to indent the HEA substrate using a velocity of 0.5 μm/s. The Berkovich indenter tip was prescribed with a peak load of 10 N in 4 s and the load was held for 20 s followed by unloading in 10 s as per the load function shown in Fig. 3.

2.2. MD simulation setup

The MD simulations were carried out using the "Large-scale Atomic/Molecular Massively Parallel Simulator" (LAMMPS) software [23]. A series of MD simulations consisted of nanoindentation on the (100), (110), (111) and polycrystalline $Ni_{25}Cu_{18.75}Fe_{25}Co_{25}Al_{6.25}$ substrates were performed. The crystal structure of the HEA substrate was built by employing special quasi-random structures (SQS) approach in the Atomsk software [24]. The schematic model of the monocrystalline and

Table 1
Detailed description of newly synthesized High-entropy alloy [16].

Novel high-entropy alloy ($Ni_{25}Cu_{18.75}Fe_{25}Co_{25}Al_{6.25}$)				
Ni	Cu	Fe	Co	Al
0.25	0.1875	0.25	0.25	0.0625
Calculated physical parameters				
ΔHmix (kJ/mol)	**ΔSmix (J/K.mol)**	**VEC**	**Δχ**	**δ**
0.2656	12.689	9	0.07178	3.5973

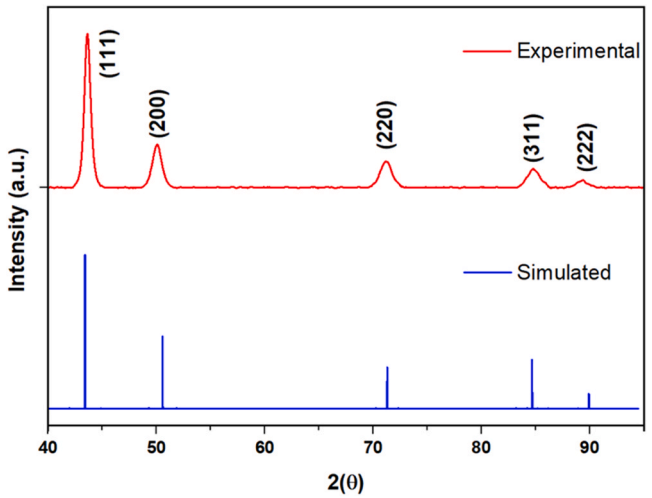

Fig. 2. : Experimental X-ray diffraction pattern along with the simulated X-ray diffraction pattern of the newly synthesised high entropy alloy $Ni_{25}Cu_{18.75}Fe_{25}Co_{25}Al_{6.25}$.

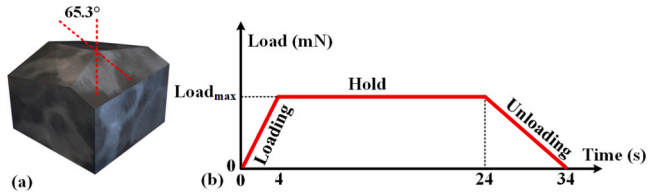

Fig. 3. (a) Schematic of the Berkovich indenter tip and (b) load function used for the nanoindentation.

polycrystalline HEA built in this work are shown in Fig. 4. The polycrystalline HEA specimen of size 36.1 nm × 36.1 nm × 35.9 nm containing 30 no. of grains was modelled and visualised using Open Visualization Tool (OVITO) [25] as shown in Fig. 4(b) and Fig. 4(c). The post processing of LAMMPS data was performed with an automated "dislocation extraction algorithm" (DXA) algorithm [26] to identify crystal defects, origins of dislocations and their Burgers Vector. The MD simulations were performed using the NVE ensemble at an equilibrated temperature of 300 K by applying the Nose–Hoover method [27] for 30 ps. The boundary conditions were set to be p, s and p type in X, Y and Z directions respectively [28,29].

For robust description of the chemical atoms containing five types of atoms (Ni, Cu, Fe, Co and Al), an EAM potential developed by Zhou et al. [30] was used. Further details of the process parameters used to perform the MD simulation of $Ni_{25}Cu_{18.75}Fe_{25}Co_{25}Al_{6.25}$ in this work are provided in Table 2.

Table 2
Detailed parameters used to perform the MD simulation of nanoindentation of $Ni_{25}Cu_{18.75}Fe_{25}Co_{25}Al_{6.25}$ HEA.

Dimensions of the HEA substrate	36.1 nm × 35.9 nm × 36.1 nm in X, Y and Z directions, respectively
Number of atoms in the HEA workpiece	~4000,000
Free travelling initial distance between the indenter and the HEA surface	0.3 nm
Depth of indentation	1.5 nm
Indentation velocity	10 m/s
Indenter diameter	8 nm
Substrate setup for indent simulations	Case 1: (100) oriented on the Y axis. Case 2: (110) oriented on the Y axis Case 3: (111) oriented on the Y axis Case 4: Polycrystalline sample with 30 no. of grains (each grain nearly ~14.4 nm diameter)
Ensemble used in the simulation	NVE at 300 K
Boundary conditions	p s p in X, Y and Z directions respectively
Indenter type	An imaginary spherical shaped rigid indenter of radius R= 4 nm described by a repulsive force constant $F(r) = K(r\text{-}R)^2$ where K is the force constant (1 KeV/Å^3), R is the radius of the spherical indenter and r is the distance of atom of the work piece from the centre of the spherical indenter. This implies that F(r) remains repulsive if R > r or becomes zero otherwise.
Timestep used for the calculation	1 fs

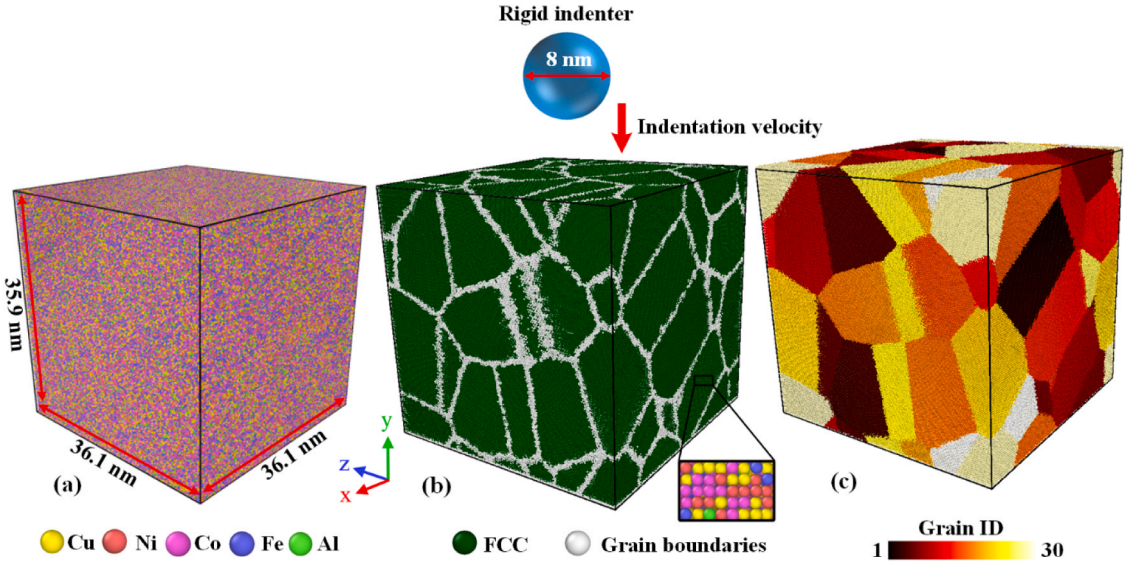

Fig. 4. : (a) Monocrystalline $Ni_{25}Cu_{18.75}Fe_{25}Co_{25}Al_{6.25}$ HEA model (b) polycrystalline $Ni_{25}Cu_{18.75}Fe_{25}Co_{25}Al_{6.25}$ HEA model (c) Identification of individual grains in the polycrystalline HEA sample.

3. Results and discussions

3.1. P-h (Load-displacement) plots of nanoindentation

3.1.1. P-h plots obtained from the MD simulation

The *P-h* curves obtained from the MD simulation for the (100), (110), (111) and polycrystalline HEA obtained from the simulated nanoindentation are shown in Fig. 5. A total displacement of 1.8 nm can be seen which include 0.3 nm of free travel before the indenter touches the substrate and then advances into the substrate by 1.5 nm depth. From Fig. 5, the loading and unloading processes were accompanied by several pop-in and pop-out events. Fig. 5 also revealed that the peak loading forces at 1.5 nm indent depth were 1241.8 nN, 511.5 nN, 1286.1 nN and 466 nN for the (100), (110) (111) monocrystalline and polycrystalline HEA substrate respectively. The lowest peak load of 466 nN observed in poly HEA can be attributed to the easy slippage and deformation of the grain boundaries (GBs). The observation of GBs was extensively examined and is discussed in the next sections. The residual depth of indentation $h_f$indicated the extent of permanent plastic deformation of the HEA substrate during the timescale of the simulation.

The $h_{\max}$ signifies the maximum depth of indentation. The value ($h_f/h_{\max}$) was calculated for each case. It can be seen that the polycrystalline HEA showed the minimum $h_f/h_{\max}$ of 0.398 while the (100), (110) and (111) monocrystalline HEA substrate showed this ratio to be 0.733, 0.493 and 0.721, respectively.

To quantify the reduced modulus of the HEA substrate (E_s), Oliver and Pharr (O&P) method was used [31]:

$$E_r = \frac{1}{\beta}\frac{\sqrt{\pi}}{2}\frac{S}{\sqrt{A}} \tag{1}$$

$$\frac{1-\upsilon_{specimen}{}^2}{E_{specimen}} = \frac{1}{E_r} - \frac{1-\upsilon_{indenter}{}^2}{E_{indenter}} \tag{2}$$

where E_r is the reduced elastic modulus, S is the slope of the top 1/3rd part of the unloading curve, $\beta = 1$ a constant for spherical indenter, A is the projected area (m^2) which varies with the depth of indentation. For this work, since a purely repulsive indenter was used, the value of $E_{indenter}$ is infinite; the equation to obtain $E_{specimen}$ then simplifies to:

$$E_{specimen} = E_r \times (1-\upsilon_{specimen}{}^2) \tag{3}$$

where the value of $\upsilon_{specimen}$ (Poisson's ratio) was taken as 0.26 for the $Ni_{25}Cu_{18.75}Fe_{25}Co_{25}Al_{6.25}$ substrate [32]. The estimated projected contact area was computed by employing geometry-based area function approach [33], as shown in Eq. (4).

$$A = \pi[h(2R-h)] \tag{4}$$

where R is the radius of the indenter and h is the instantaneous displacement of the indenter.

Additionally, hardness is a measure of a material's resistance to plastic deformation which can be obtained as

$$H = \frac{P_h}{A} \tag{5}$$

where P_h represents the loading force during loading process.

The MD results obtained from the simulations revealing the length scale dependent elastic modulus and nanoindentation hardness are shown in Fig. 6. Fig. 6(a) indicated that the polycrystalline HEA substrate showed the lowest magnitude of elastic modulus while the (111) monocrystalline HEA showed the highest elastic modulus. In Fig. 6(b), following the same order, the lower nanoindentation hardness was shown by the polycrystalline substrate whilst the (111) orientation showed the highest hardness with (110) orientation being the softer orientations across the three major crystallographic orientations.

It may be noted that in the MD simulations performed here, a purely repulsive indenter was used so the values of indentation hardness and

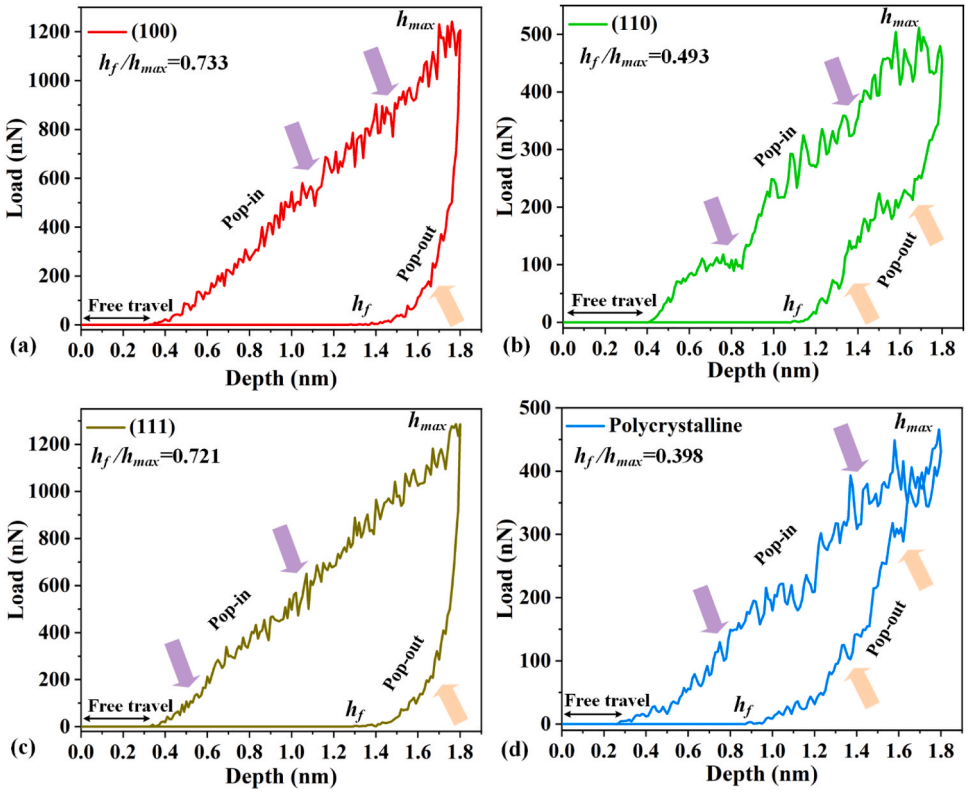

Fig. 5. *P-h* curves obtained from the MD simulation for the HEA (a) (100) orientation (b) (110) orientation (c) (111) orientation and (d) polycrystalline HEA. Violet arrows and orange arrows refer to the Pop-in and Pop-out events respectively.

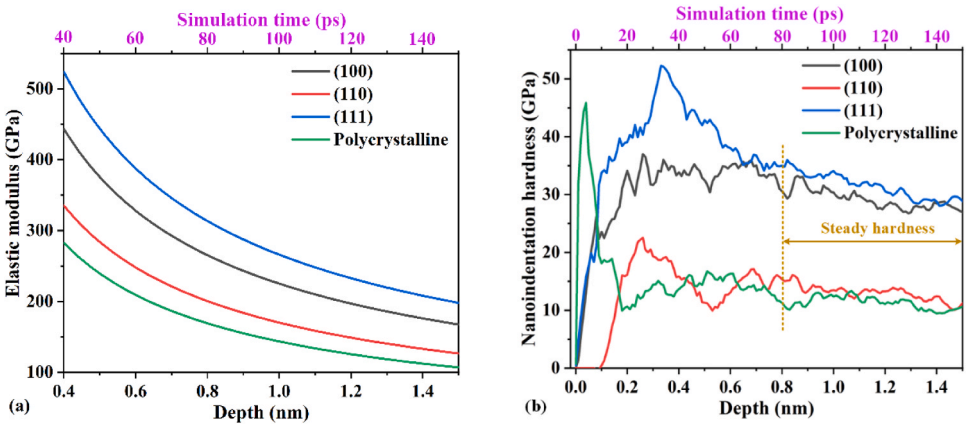

Fig. 6. (a) Variation in the elastic modulus and (b) nanoindentation hardness of $Ni_{25}Cu_{18.75}Fe_{25}Co_{25}Al_{6.25}$ HEA obtained from the MD simulations.

modulus extracted from the simulations are not comparable to the experimental values. This is because as opposed to a diamond indenter, an imaginary repulsive indenter had infinite modulus and a frictionless repulsive surface. This aspect was already reviewed by the authors in their previous work [33] so the value of elastic modulus and hardness obtained from a pure repulsive indenter is only indicative but the approximation about the dislocation and plasticity mechanisms obtained from MD are still valuable to understand the origins of the

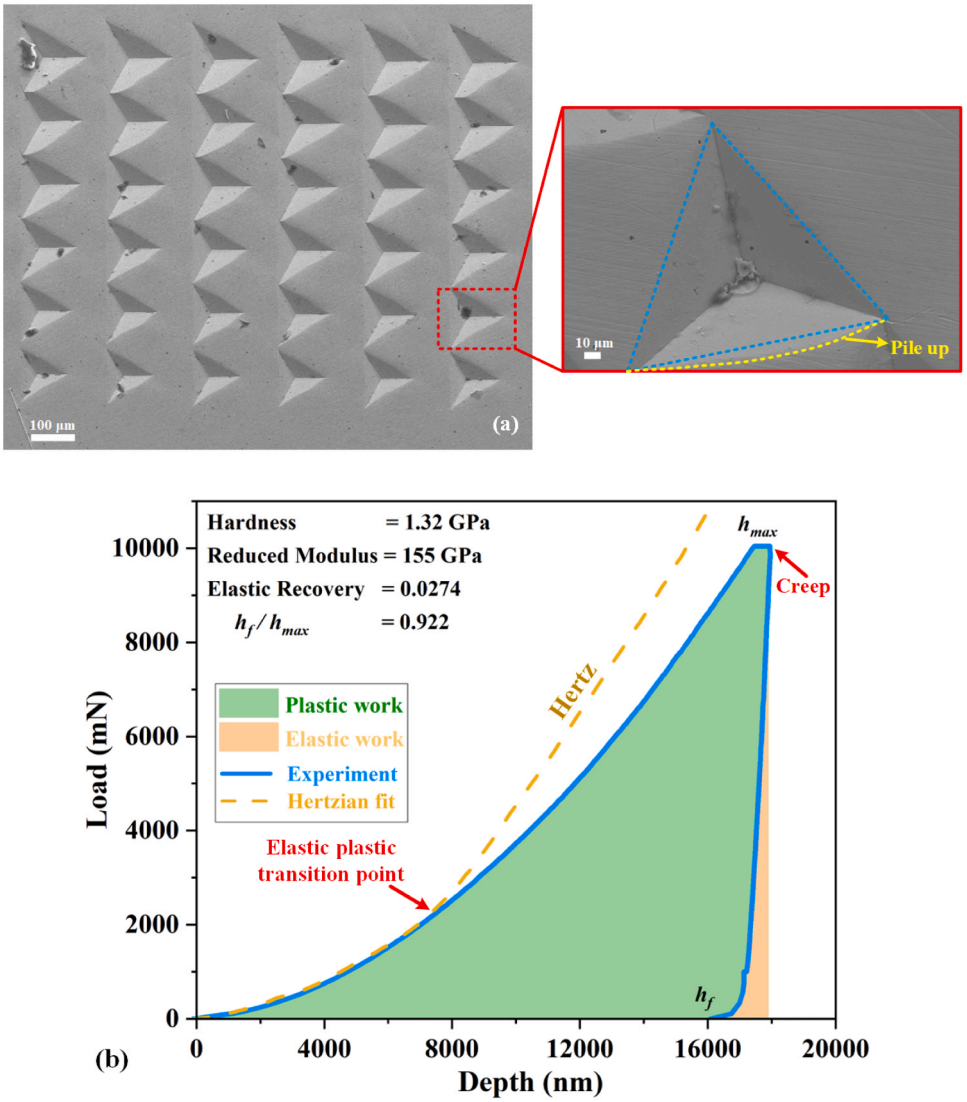

Fig. 7. (a) SEM of indentation array performed on the polycrystalline HEA (b) Experimental *P–h* plot and Hertzian fit on the $Ni_{25}Cu_{18.75}Fe_{25}Co_{25}Al_{6.25}$ polycrystalline substrate highlighting elastic and plastic work involved in the HEA indentation.

plasticity mechanisms.

3.1.2. P-h plot and the anisotropic pile up seen from the nanoindentation experiments

The P-h plot from the nanoindentation experiments performed on the indigenously synthesised polycrystalline HEA composition $Ni_{25}Cu_{18.75}Fe_{25}Co_{25}Al_{6.25}$ HEA [34] is been shown in Fig. 7. An array of 36 indents was made in the HEA sample as shown in Fig. 7(a). At a peak load of 10 N, the maximum indentation depth was about ~18 μm. No sink in behaviour was noticed but anisotropic pileup only along one edge of the nanoindentation edge in the SEM imaging of the nanoindentation topography can be seen from Fig. 7(a). The departure of the blue line to the yellow line (Fig. 7(a)) only on one of the three indented edges suggest strong anisotropy in the pile-up behaviour of HEA. The HEA revealed a reduced elastic modulus of 155 GPa and nanoindentation hardness of 1.32 GPa. h_f/h_{max} is a useful parameter to predict pile-up or sink-in behaviour, where a ratio above 0.7 indicates pile-up behaviour and a ratio below 0.7 suggests sink-in behaviour [35–37]. In case of the newly synthesised $Ni_{25}Cu_{18.75}Fe_{25}Co_{25}Al_{6.25}$, the experimental h_f/h_{max} was 0.922, as indicated in Fig. 7(b). This value confirms pile up behaviour during nanoindentation. A Hertzian curve was fitted to identify the elastic-plastic transition point. This point coincides at an indentation depth of ~8 μm which is demonstrated in Fig. 7(b). The area of plastic deformation zone was significantly higher than the area under the elastic deformation zone which is a clear indication that the newly synthesised $Ni_{25}Cu_{18.75}Fe_{25}Co_{25}Al_{6.25}$ HEA deformed predominantly in the plastic mode with minimum elastic recovery. It should be noted that the experimental sample indented was a polycrystalline HEA.

3.2. Anisotropy in HEA deformation obtained from the MD simulations

The residual indentation showed strong anisotropy on the (100), (110), (111) orientations as well as on the polycrystalline HEA shown in Fig. 8. The (100) HEA showed clear 4-fold symmetry atomic pileup (see Fig. 8(a)) along the ⟨011⟩, ⟨$0\bar{1}\bar{1}$⟩, ⟨$0\bar{1}1$⟩ and ⟨$01\bar{1}$⟩ directions, which is consistent with the previous report for the Fe-Ni-Cr-Co-Cu high-entropy alloy [20]. The (110) monocrystalline setup showed evenly distributed deformation shown in Fig. 8(b) with somewhat a 4-fold symmetry. In the case of (111) orientation, material flow and pileup shown in Fig. 8(c) did not indicate any clear preferential direction of deformation. Interestingly, for the polycrystalline HEA model, the 4-fold or 3-fold symmetry atomic pileup was less clearer due to the interaction of several grains which can be seen from Fig. 8(d). To further study this, the polycrystalline dump file was post-processed by removing the top lattice layers using the polyhedral template matching algorithm within OVITO which leaves a clear visibility of the individual grains as shown in Fig. 9.

For ease of understanding, the polycrystalline configuration has been compared pre and post indentation deformation by bringing an EBSD equivalent colour scheme. It can be seen from Fig. 9 that the indenter made contact in the region which is at the intersection of several grains with orientations (310), (111), (101) and (210). As opposed to a perfect spherical symmetry, the lines of plastic deformation can be seen to be

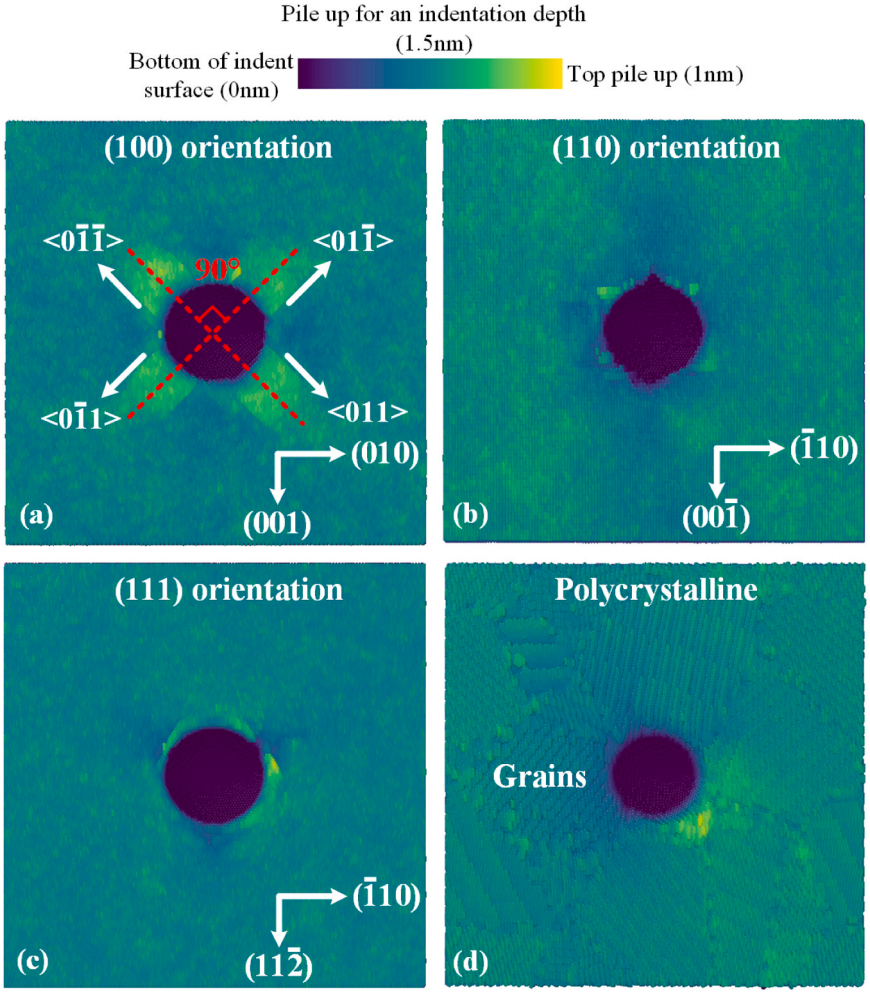

Fig. 8. Top view of the residual indentation of the $Ni_{25}Cu_{18.75}Fe_{25}Co_{25}Al_{6.25}$ substrate on the (a) (100) orientation (b) (110) orientation (c) (111) orientation and (d) polycrystalline HEA (see Fig. 9 for further analysis).

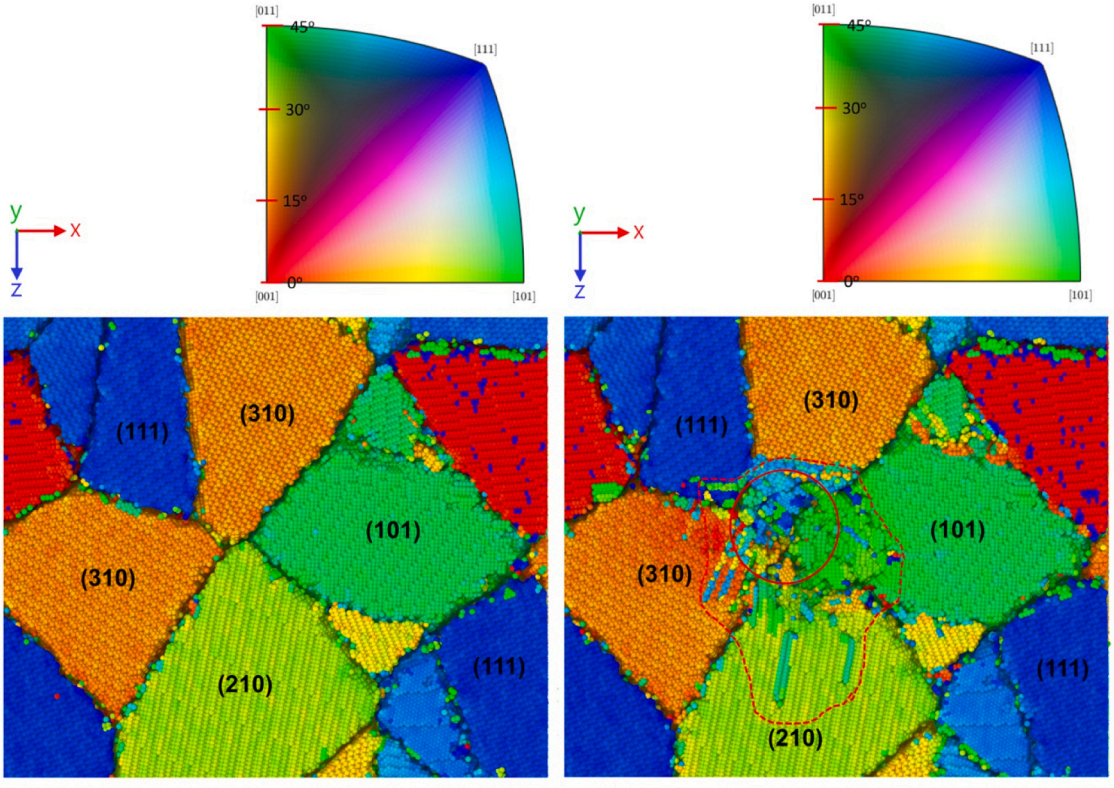

Fig. 9. The state of various grains (a) before indentation and (b) after indentation on the polycrystalline HEA.

traversing through these grains carrying different propensity of deformation. Of those grains, the (210) orientation can be seen to be affected the most showing that the extent of dislocation propagation has affected a good half part of the grain, thus confirming that this orientation is most amenable compared to the other three grains in the ease of its plastic deformation.

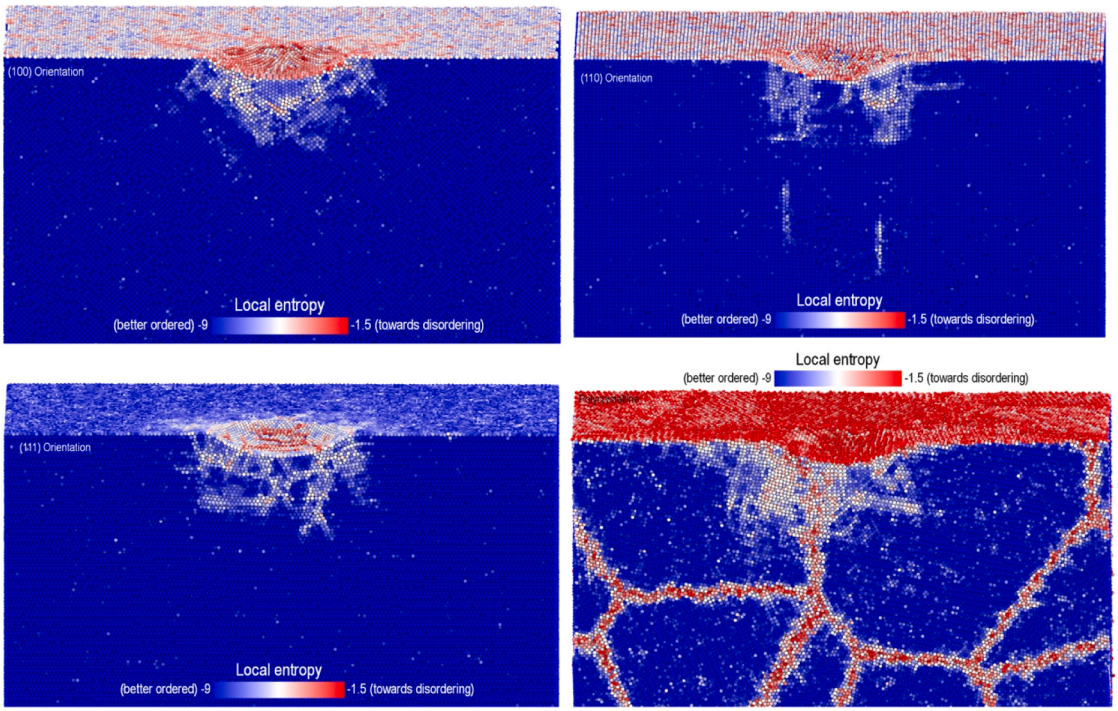

Fig. 10. The measurement of local entropy for nanoindentation on (100) monocrystalline, (110) monocrystalline, (111) monocrystalline and polycrystalline HEA.

3.3. Mechanism of plastic deformation in $Ni_{25}Cu_{18.75}Fe_{25}Co_{25}Al_{6.25}$ HEA

The entropy based fingerprint calculation within OVITO is highlighted in Fig. 10 which distinguishes ordered and disordered structure. When the value of location entropy is more negative, then it is better ordered [38]. In the case of HEA indentation, the degree of disoardering can be seen to grow in the areas affected by the stress exerted by the indenter as well as in the grain boundaries. Also, the growth of the dislocation loops deeper on the (110) orientation can be seen to change the measure of local entropy which in other words indicates the local disordering in the crystalline structure of FCC HEA. An extended analysis of these disordered structures was made using the CAT algorithm which is discussed further.

The evolution of microstructure of HEA during nanoindentation process is shown by Figs. 11, 12, 13 and 14 revealing various atomic movements indicating mechanisms of reversible and inelastic behaviour of HEA at indentation depths of 0.5 nm, 1.5 nm and after unloading. During the nanoindentation process several types of dislocations such as the $1/2 < 110 >$ perfect dislocation, $1/6 < 112 >$ Shockley dislocation, $1/6 < 110 >$ Stair-rod dislocation, $1/3 < 100 >$ Hirth dislocation and $1/3 < 111 >$ Frank dislocation were seen to emerge which are shown in Fig. 11 and Fig. 13. These were accompanied by multiple shear dislocation loops leading to a forest of dislocations after unloading the indentation load as also reported experimentally through TEM observations [39].

On indentation of the (110) orientation, a "lasso" type dislocation loop can be seen to emerge, which was not evidenced in any other case of indentation [40,41]. The (110) orientation showed multiple shear loops which were seen to advance under the stress caused by the indenter into the HEA material by the advancement of their edge components. The formation process of "lasso" type dislocation loop is explained further using the analytical model of dislocation evolution through Fig. 12, where a octahedron dislocation loop is used to indicate the formation process of "lasso" type dislocation loop. Fig. 12(a) shows the shear loop formed on the $(\bar{1}0\bar{1})$ orientation that propagates along with [111] slip direction. The continuous cross-over of screw components along the [111] direction in two families of slip planes {110} and {111} ends up forming the octahedron "lasso" type dislocation loop, also called "lasso action", which can be seen in more details from Fig. 12(b-f).

The dislocations for the (111) orientation was mostly $1/6 < 112 >$ Shockley, $1/6 < 110 >$ Stair-rod and $1/3 < 100 >$ Hirth. Note that the Hirth dislocation can result from reactions between Shockley dislocations as $1/6[\bar{1}2\bar{1}] + 1/6[\bar{1}2\bar{1}] = 1/3[\bar{1}00]$ and Frank dislocation can result from reactions of Stair-rod and Shockley, e.g., $1/6[011] + 1/6[211] = 1/3[111]$, Hirth dislocations are also known as Hirth locks [42] and Frank dislocations are known as Lomer–Cottrell (LC) locks [43].

A typical FCC structure has 12 non-equivalent partial dislocation slip systems $\langle 110 \rangle/2$-{111}. However, not all these slip systems are operative during contact loading experiment such as nanoindentation. Based on tensor rotation, we can convert the applied shear stress (~5–6 GPa) to each of the slip systems. The slip systems with the maximum conversion factors (analogous to Schmid factor) are operative. We found that the (010) orientation would have eight most likely operative slip systems $[101]/2$-$(\bar{1}11)$, $[0\bar{1}1]/2$-$(\bar{1}11)$, $[101]/2$-$(11\bar{1})$, $[011]/2$-$(11\bar{1})$, $[011]/2$-$(\bar{1}1\bar{1})$, $[10\bar{1}]/2$-$(\bar{1}1\bar{1})$, $[0\bar{1}1]/2$-(111), $[\bar{1}01]/2$-(111) with a conversion factor of 0.41, the (110) orientation has four most likely operative slip systems $[110]/2$-$(1\bar{1}1)$, $[1\bar{1}0]/2$-$(11\bar{1})$, $[110]/2$-$(\bar{1}1\bar{1})$, $[1\bar{1}0]/2$-(111) with a conversion factor of 0.82, and the (111) orientation has one most likely operative slip systems $[1\bar{1}0]/2$-(111) with a conversion factor of 1.00, two second likely operative slip systems $[110]/2$-$(\bar{1}11)$, $[110]/2$-$(1\bar{1}1)$ with a conversion factor of 0.87, and four most likely operative slip systems $[101]/2$-$(1\bar{1}1)$, $[011]/2$-$(\bar{1}1\bar{1})$, $[0\bar{1}1]/2$-(111), $[\bar{1}01]/2$-(111) with a conversion factor of 0.50. Note that during the (010) indentation, every slip vector is activated on two slip planes, for instance, the $[101]/2$ vector is activated on the $(\bar{1}11)$ and $(11\bar{1})$ planes in the $[101]/2$-$(\bar{1}11)$ and $[101]/2$-$(11\bar{1})$ slip systems. This feature is not present in the other orientations.

In terms of the crystal defects, Fig. 13 identifies these defects. They consist of FCC intrinsic stacking faults (ISF) resembling two atomic layers of hcp coordination, adjacent intrinsic stacking faults (quad faults and resembles as four atomic layers of hcp coordination), coherent $\sum 3$ twin boundary and a coherent twin boundary next to an intrinsic stacking fault (triple fault) resembling three atomic layers of hcp coordination. The evolution of microstructure of monocrystalline HEA and polycrystalline HEA is demonstrated in Fig. 14 during nanoindentation process, where the green color atoms refer to the FCC microstructure, white color atoms mean disordered atoms and the red colour atoms highlights stacking faults. At indentation depth of 0.5 nm, FCC microstructure becomes disordered and stacking faults appeared in the deformation zone. At a deeper depth of 1.5 nm, more stacking faults were observed. The stacking faults were formed on both sides of deformed area for the (100) HEA substrate while a number of stacking faults extend deeply along the parallel to direction of the tool for the (110) and (111) HEA substrate. During the unloading process, as the material recover occurs, some of the stacking faults reverses back and disappears. Furthermore, Fig. 14 highlights that the presence of grain boundary obstructs the growth and propagation of shear loops leading to form a complex and concentrated junction of stacking faults in the indented area. Thus, in the case of (110) and polycrystalline HEA substrates, the elastic work in the indentation hysteresis loop was seen to be larger than the (100) and the (111) orientations.

4. Conclusions

The paper report novel insights into the anisotropic plastic deformation mechanisms of a high entropy alloy (HEA) with composition $Ni_{25}Cu_{18.75}Fe_{25}Co_{25}Al_{6.25}$. In line with the Thermo-Calc prediction, the XRD experiments revealed that this HEA composition stabilises in FCC phase. Nanoindentation experiments using a Berkovich indenter under load-controlled conditions showed its hardness and reduced modulus to be about 1.32 GPa and 155 GPa respectively. A broad list of conclusions from this study can be summarised as below:

1. The (100) orientation monocrystalline showed atomic pileup with a clear 4-fold symmetry. The value of $h_f/h_{\max}$ from the MD simulations on monocrystalline HEA was consistently found to be larger than 0.7 which suggested pile-up behaviour to dominate during indentation of HEA and sink-in behaviour to be unlikely. In the case of (110) and polycrystalline HEA substrates, the elastic work in the indentation hysteresis loop was seen to be larger than the (100) and the (111) orientations. It was learned that the (110) orientation was softer while the (111) monocrystalline HEA showed the highest elastic modulus and hardness.
2. A "lasso" type dislocation loop forms due to the interaction of two shear loops on the (110) orientation whereas the other orientations were seen to deform by the cross-over of shear loops. The dislocations nucleated and propagated were mostly $1/6 < 112 >$ Shockley, $1/6 < 110 >$ Stair-rod and $1/3 < 100 >$ Hirth Locks. The Hirth dislocation was seen to be resulting from the reactions between Shockley dislocations as $1/6[\bar{1}2\bar{1}] + 1/6[\bar{1}2\bar{1}] = 1/3[\bar{1}00]$ and Frank dislocation (as Lomer–Cottrell (LC) locks) was the result of reaction between Stair-rod and Shockley, e.g., $1/6[011] + 1/6[211] = 1/3[111]$.
3. The defects accompanying these dislocations in the sub-surface were identified to be FCC intrinsic stacking faults (ISF), adjacent intrinsic stacking faults (quad faults), coherent $\sum 3$ twin boundary and a coherent twin boundary next to an intrinsic stacking fault (triple fault). From EBSD analysis applied to the MD data, an acute information learned was that the (210) orientation and

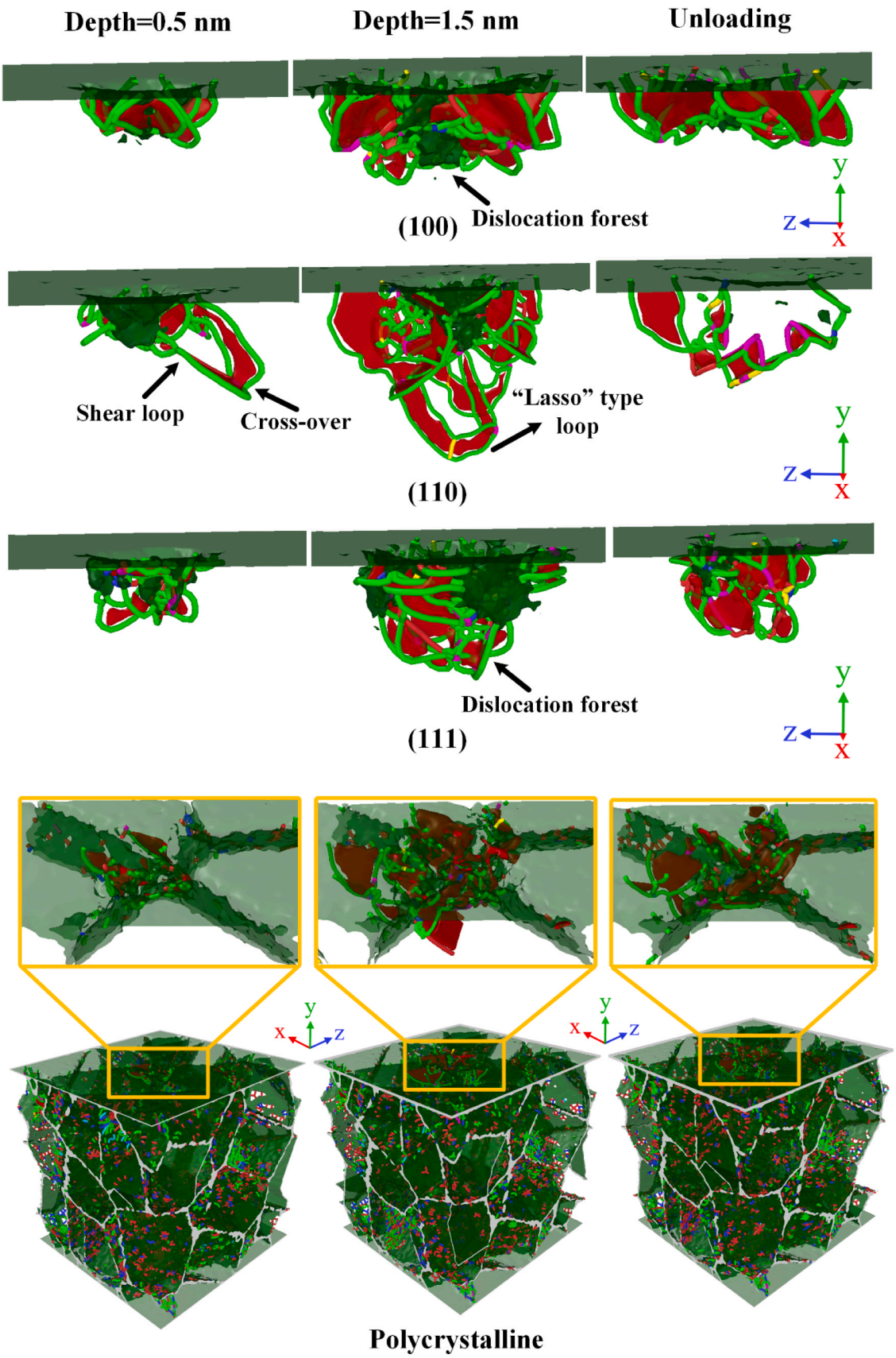

Fig. 11. The evolution of dislocation nucleation and movement at the 0.5 nm depths, 1.5 nm depths and the unloading stage for (100) monocrystalline, (110) monocrystalline, (111) monocrystalline and polycrystalline structure.

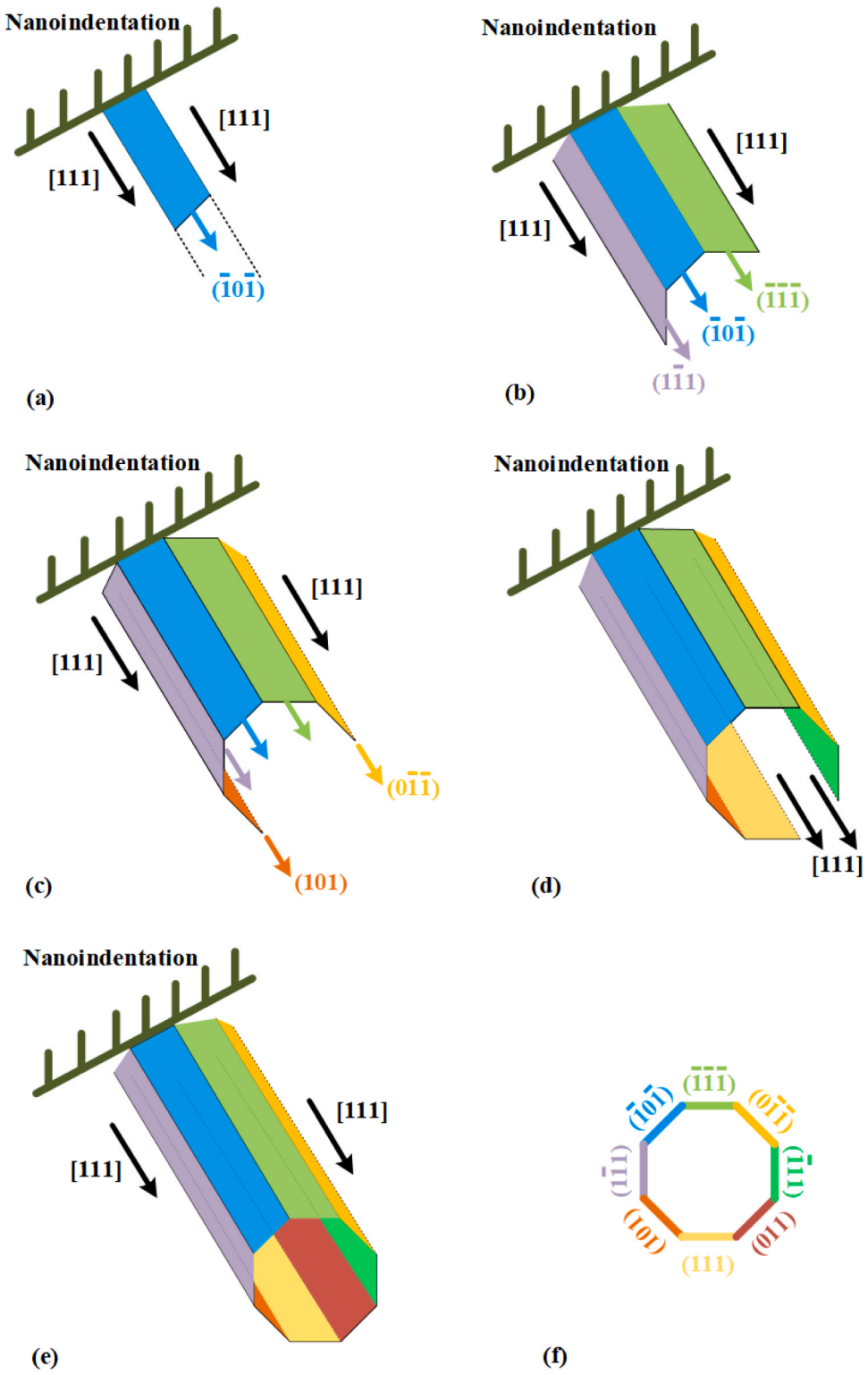

Fig. 12. Analytical models of dislocation evolution (a) Emission of shear loop (b-d) Cross-over of screw components (e-f) Formation of octahedron "lasso" type dislocation loop.

the< 110 > family of directions were seemed to be preferable for the plastic deformation in FCC phased HEAs.

CRediT authorship contribution statement

Pengfei Fan: MD simulation data analysis and drafting of the manuscript. **Nirmal Kumar Katiyar:** Experimental synthesis of the alloy and experimental nanoindentation. **Muhammad Arshad:** Thermo-Calc analysis. **Mingwen Bai:** Thermo-calc analysis. **Hui Mao**: Proof reading of the manuscript. **Saurav Goel:** Project acquisition, supervision, editing and proof reading.

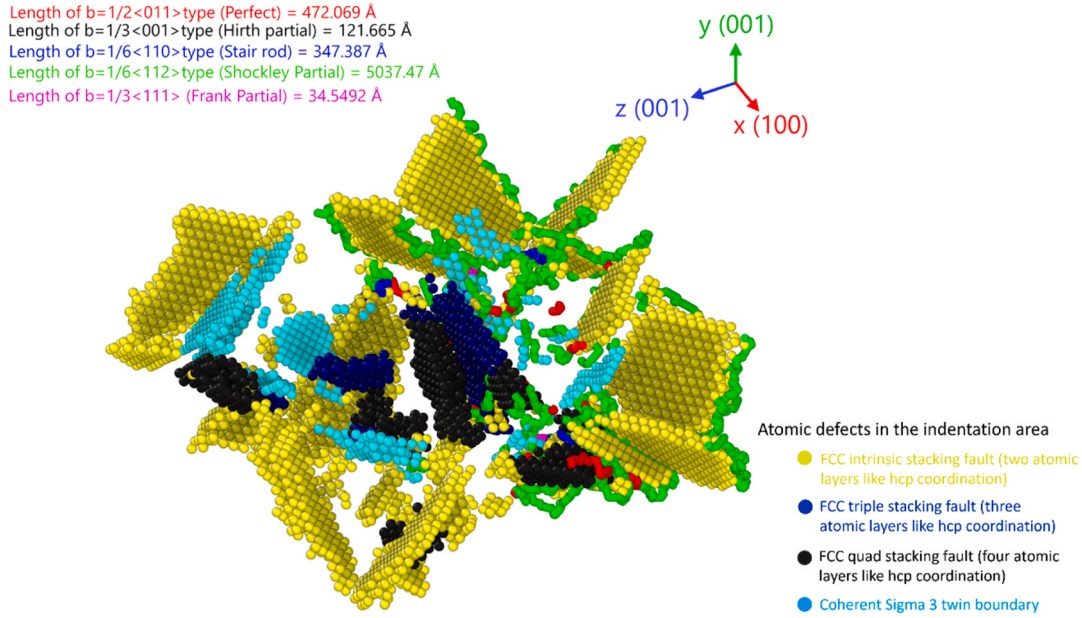

(a) Dislocation and defect atom types after indentation on (100) monocrystalline HEA showing several nested "shear loops"

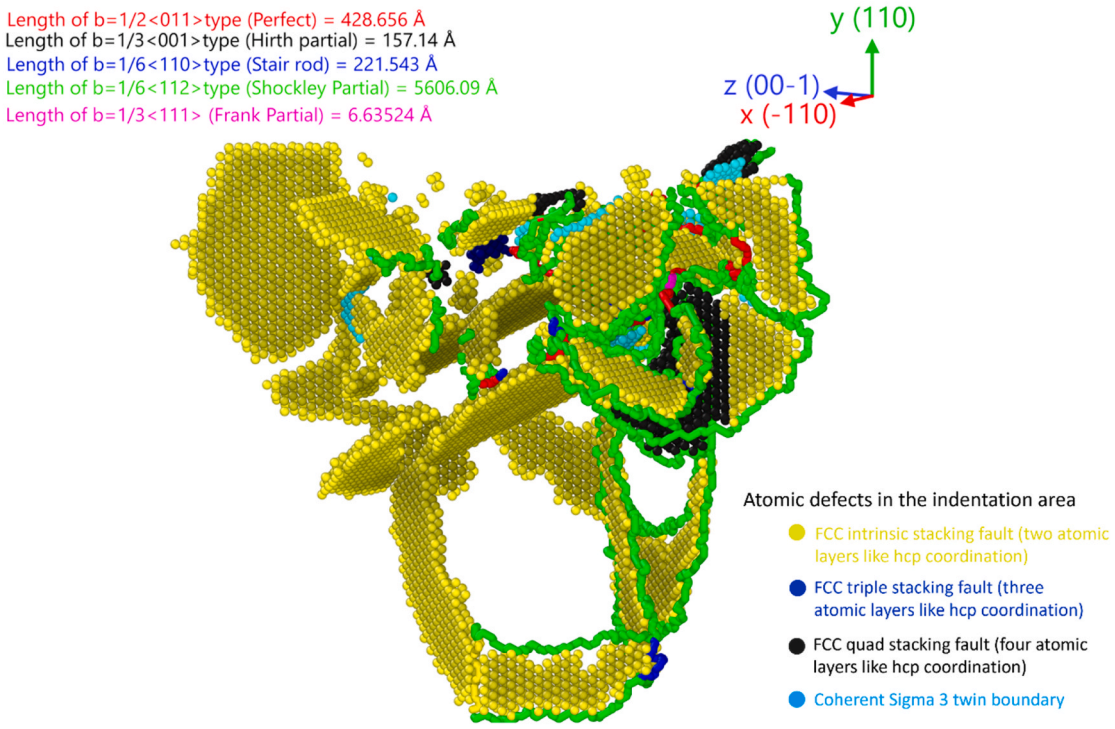

(b) Dislocation and defect atom types after indentation on (110) monocrystalline HEA showing "lasso-like" dislocation loop

Fig. 13. The demonstration of dislocation nucleation and defect atom types after indentation for (a) (100) monocrystalline, (b) (110) monocrystalline, (c) (111) monocrystalline and (d) Dislocation length.

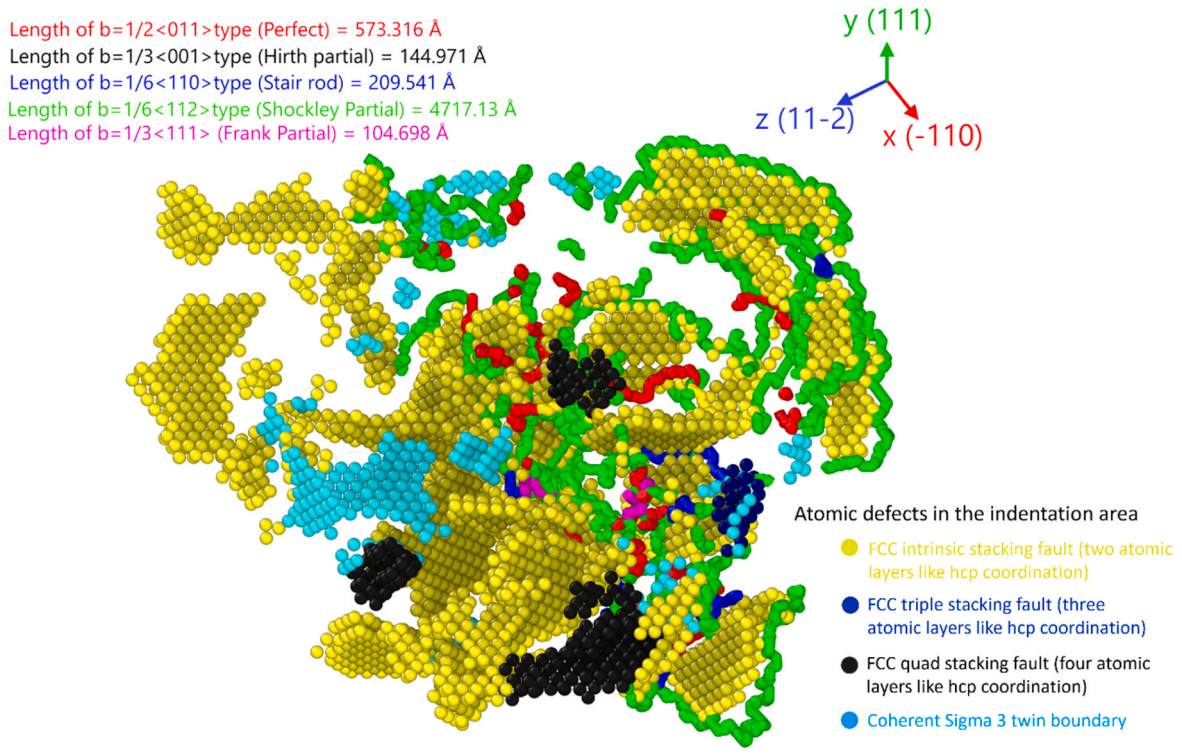

(c) Dislocation and defect atom types after indentation on (111) monocrystalline HEA

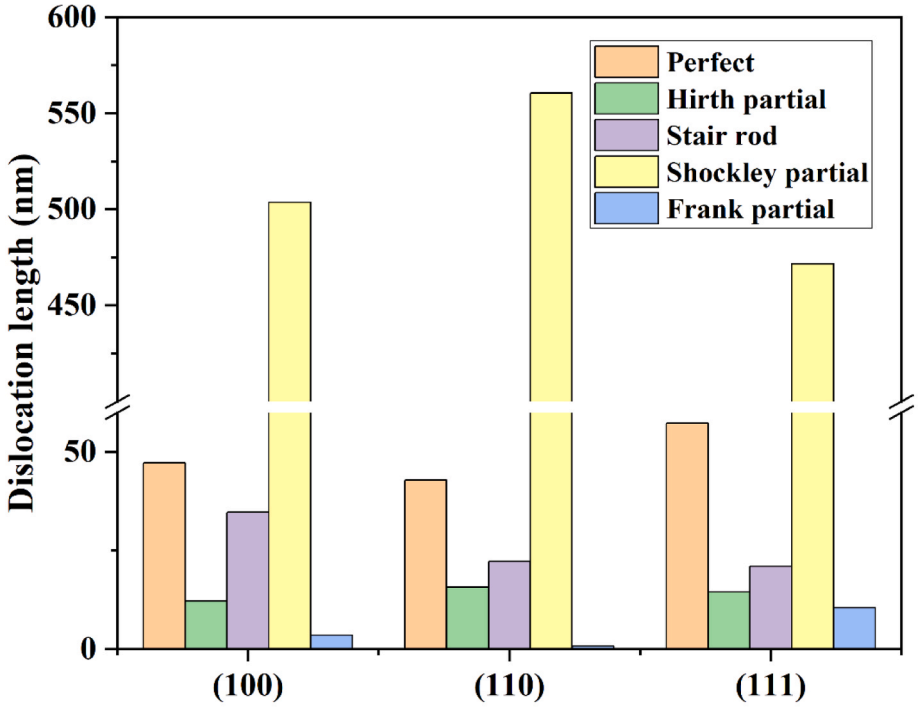

(d) Dislocation length after indentation on different orientations monocrystalline HEA

Fig. 13. (*continued*).

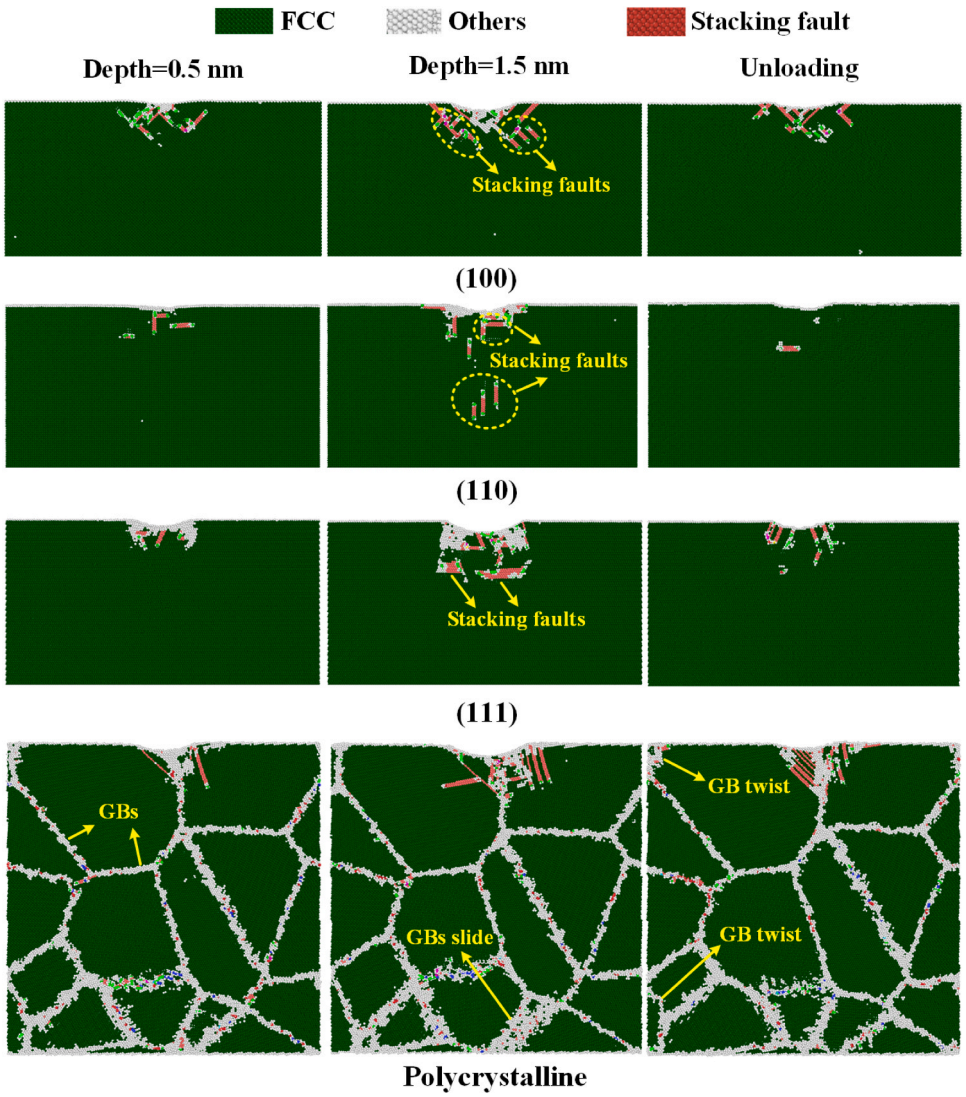

Fig. 14. The evolution of microstructure at depths of 0.5 nm, 1.5 nm and after unloading.

Declaration of Competing Interest

The authors declare that they have no known competing financial interests or personal relationships that could have appeared to influence the work reported in this paper.

Data Availability

Data will be made available on request.

Acknowledgement

SG would like to acknowledge the financial support provided by the UKRI via Grants No. EP/S036180/1 and EP/T024607/1, Hubert Curien Partnership Programme from the British Council and the International Exchange Cost Share award by the Royal Society (IEC\NSFC\223536). This work also accessed the Isambard Bristol, UK supercomputing service via Resource Allocation Panel (RAP), Kittrick HPC at LSBU and Param Kamrupa HPC based at Guwahati, India.

References

[1] J. Ren, et al., Strong yet ductile nanolamellar high-entropy alloys by additive manufacturing, Nature vol. 608 (7921) (2022) 62–68.
[2] S. Chen, et al., Simultaneously enhancing the ultimate strength and ductility of high-entropy alloys via short-range ordering, Nat. Commun. vol. 12 (1) (2021) 1–11.
[3] E. Ma, X. Wu, Tailoring heterogeneities in high-entropy alloys to promote strength–ductility synergy, Nat. Commun. vol. 10 (1) (2019) 1–10.
[4] W. Li, P.K. Liaw, Y. Gao, Fracture resistance of high entropy alloys: a review, Intermetallics vol. 99 (April) (2018) 69–83.
[5] C. Chen, S. Pang, Y. Cheng, T. Zhang, Microstructure and mechanical properties of Al20-xCr20+0.5xFe20Co20Ni20+0.5x high entropy alloys, J. Alloy. Compd. vol. 659 (2016) 279–287.
[6] P.L.J. Conway, T.P.C. Klaver, J. Steggo, E. Ghassemali, High entropy alloys towards industrial applications: High-throughput screening and experimental investigation, no. November 2021, Mater. Sci. Eng. A vol. 830 (2022), 142297.
[7] W. Ye, et al., Microstructure and tribological properties of in-situ carbide/CoCrFeNiMn high entropy alloy composites synthesized by flake powder metallurgy (no. January), Tribol. Int. vol. 181 (2023), 108295.
[8] Z. Li, S. Zhao, R.O. Ritchie, M.A. Meyers, Mechanical properties of high-entropy alloys with emphasis on face-centered cubic alloys, no. March 2018, Prog. Mater. Sci. vol. 102 (2019) 296–345.
[9] S. Gorsse, D.B. Miracle, O.N. Senkov, Mapping the world of complex concentrated alloys, Acta Mater. vol. 135 (2017) 177–187.
[10] Y. Ren, et al., Friction-induced rapid amorphization in a wear-resistant (CoCrNi)88Mo12 dual-phase medium-entropy alloy at cryogenic temperature (no. June), Compos. Part B Eng. vol. 263 (2023) (no. June).
[11] Q. Zhou, et al., Design and characterization of metallic glass/graphene multilayer with excellent nanowear properties, Friction vol. 10 (11) (2022) 1913–1926.
[12] E.J. Pickering, A.W. Carruthers, P.J. Barron, S.C. Middleburgh, D.E.J. Armstrong, A.S. Gandy, High-entropy alloys for advanced nuclear applications, Entropy vol. 23 (1) (2021) 1–28.
[13] H.X. Guo, C.Y. He, X.L. Qiu, Y.Q. Shen, G. Liu, X.H. Gao, A novel multilayer high temperature colored solar absorber coating based on high-entropy alloy

MoNbHfZrTi: Optimized preparation and chromaticity investigation, no. June 2019, Sol. Energy Mater. Sol. Cells vol. 209 (2020), 110444.
[14] X. Yan, Y. Zhang, Functional properties and promising applications of high entropy alloys, Scr. Mater. vol. 187 (2020) 188–193.
[15] S. Dixit, et al., Refractory high-entropy alloy coatings for high-temperature aerospace and energy applications, J. Therm. Spray. Technol. vol. 31 (4) (2022) 1021–1031.
[16] S. Singh, N.K. Katiyar, S. Goel, S.N. Joshi, Phase prediction and experimental realisation of a new high entropy alloy using machine learning, Sci. Rep. vol. 13 (1) (2023), 4811.
[17] N.K. Katiyar, G. Goel, S. Goel, Emergence of machine learning in the development of high entropy alloy and their prospects in advanced engineering applications, Emergent Mater. vol. 4 (6) (2021) 1635–1648.
[18] S. Goel, X. Luo, A. Agrawal, R.L. Reuben, Diamond machining of silicon: A review of advances in molecular dynamics simulation, Int. J. Mach. Tools Manuf. vol. 88 (2015) 131–164.
[19] D.Q. Doan, T.H. Fang, T.H. Chen, Microstructure and composition dependence of mechanical characteristics of nanoimprinted AlCoCrFeNi high-entropy alloys, Sci. Rep. vol. 11 (1) (2021) 1–19.
[20] C.J. Ruestes, D. Farkas, Dislocation emission and propagation under a nano-indenter in a model high entropy alloy, no. September 2021, Comput. Mater. Sci. vol. 205 (2022), 111218.
[21] J.O. Andersson, T. Helander, L. Höglund, P. Shi, B. Sundman, Thermo-Calc & DICTRA, computational tools for materials science, Calphad Comput. Coupling Phase Diagr. Thermochem vol. 26 (2) (2002) 273–312.
[22] J.E. Saal, I.S. Berglund, J.T. Sebastian, P.K. Liaw, G.B. Olson, Equilibrium high entropy alloy phase stability from experiments and thermodynamic modeling, Scr. Mater. vol. 146 (2018) 5–8.
[23] S.J. Plimpton, Fast parallel algorithms for short range molecular dynamics, J. Comput. Phys. vol. 117 (1995) 1–19.
[24] P. Hirel, Atomsk: a tool for manipulating and converting atomic data files, Comput. Phys. Commun. vol. 197 (2015) 212–219.
[25] A. Stukowski, Visualization and analysis of atomistic simulation data with OVITO-the Open Visualization Tool, Model. Simul. Mater. Sci. Eng. vol. 18 (1) (2010).
[26] A. Stukowski, V.V. Bulatov, A. Arsenlis, Automated identification and indexing of dislocations in crystal interfaces, Model. Simul. Mater. Sci. Eng. vol. 20 (8) (2012).
[27] S. Nose, A unified formulation of the constant temperature molecular-dynamics methods, J. Chem. Phys. vol. 81 (1984) 511–519.
[28] S.Z. Chavoshi, S. Xu, and S. Goel, "Addressing the discrepancy of finding the equilibrium melting point of silicon using molecular dynamics simulations," *Proc. R. Soc. A Math. Phys. Eng. Sci.*, vol. 473, no. 2202, pp. 1–9, 2017.
[29] N.H. Faisal, R. Ahmed, S. Goel, Y.Q. Fu, Influence of test methodology and probe geometry on nanoscale fatigue failure of diamond-like carbon film, Surf. Coat. Technol. vol. 242 (2014) 42–53.
[30] X.W. Zhou, R.A. Johnson, H.N.G. Wadley, Misfit-energy-increasing dislocations in vapor-deposited CoFe/NiFe multilayers, Phys. Rev. B - Condens. Matter Mater. Phys. vol. 69 (14) (2004) 1–10.
[31] W.C. Oliver, G.M. Pharr, An improved technique for determining hardness and elastic modulus using load and displacement sensing indentation experiments, J. Mater. Res. vol. 7 (6) (1992) 1564–1583.
[32] A. Haglund, M. Koehler, D. Catoor, E.P. George, V. Keppens, Polycrystalline elastic moduli of a high-entropy alloy at cryogenic temperatures, Intermetallics vol. 58 (2015) 62–64.
[33] S. Goel, G. Cross, A. Stukowski, E. Gamsjäger, B. Beake, A. Agrawal, Designing nanoindentation simulation studies by appropriate indenter choices: case study on single crystal tungsten (no. April), Comput. Mater. Sci. vol. 152 (2018) 196–210.
[34] P. Fan, N.K. Katiyar, X. Zhou, S. Goel, Uniaxial pulling and nano-scratching of a newly synthesized high entropy alloy Uniaxial pulling and nano-scratching of a newly synthesized high entropy alloy (no. November), APL Mater. vol. 111118 (2022) (no. November).
[35] F.B. Kværndrup, C. Engelbrekt, Ö.C. Kücükyildiz, M.A.J. Somers, T.L. Christiansen, G. Winther, Area determination with pile-up and sink-in in nanoindentation of oxygen containing titanium (no. February), Mater. Today Commun. vol. 30 (2022) (no. February).
[36] A. Bolshakov, G.M. Pharr, Influences of pileup on the measurement of mechanical properties by load and depth sensing indentation techniques, J. Mater. Res. vol. 13 (4) (1998) 1049–1058.
[37] L. Charleux, V. Keryvin, M. Nivard, J. Guin, J. Sangleb, A method for measuring the contact area in instrumented indentation testing by tip scanning probe microscopy imaging, Acta Mater. vol. 70 (2014) 249–258.
[38] P.M. Piaggi, M. Parrinello, Entropy based fingerprint for local crystalline order, J. Chem. Phys. vol. 147 (11) (2017).
[39] S. Lee, et al., In-situ observation of the initiation of plasticity by nucleation of prismatic dislocation loops, Nat. Commun. vol. 11 (1) (2020) 1–11.
[40] T.P. Remington, et al., Plastic deformation in nanoindentation of tantalum: a new mechanism for prismatic loop formation, Acta Mater. vol. 78 (2014) 378–393.
[41] H. Xiang, H. Li, T. Fu, C. Huang, X. Peng, Formation of prismatic loops in AlN and GaN under nanoindentation, Acta Mater. vol. 138 (2017) 131–139.
[42] T. Paulauskas, et al., Atomic scale study of lomer – cottrell and hirth lock dislocations in CdTe, Microsc. Microanal. vol. 21 (1042) (2015) 2087–2088.
[43] V. Bulatov, F.F. Abraham, L. Kubin, B. Devincre, S. Yip, Connecting atomistic and mesoscale simulations of crystal plasticity, Nature vol. 391 (6668) (1998) 669–672.